Non-Bias-Limited Tracking of Spherical Particles, Enabling Nanometer Resolution at Low Magnification

Marijn T. J. van Loenhout, Jacob W. J. Kerssemakers, Iwijn De Vlaminck, and Cees Dekker*
Department of Bionanoscience, Kavli Institute of Nanoscience, Delft University of Technology, Delft, The Netherlands

ABSTRACT We present a three-dimensional tracking routine for nondiffraction-limited particles, which significantly reduces pixel bias. Our technique allows for increased resolution compared to that of previous methods, especially at low magnification or at high signal/noise ratio. This enables tracking with nanometer accuracy in a wide field of view and tracking of many particles. To reduce bias induced by pixelation, the tracking algorithm uses interpolation of the image on a circular grid to determine the *x*-, *y*-, and *z*-positions. We evaluate the proposed algorithm by tracking simulated images and compare it to well-known center-of-mass and cross-correlation methods. The final resolution of the described method improves up to an order of magnitude in three dimensions compared to conventional tracking methods. We show that errors in *x,y*-tracking can seriously affect *z*-tracking if interpolation is not used. We validate our results with experimental data obtained for conditions matching those used in the simulations. Finally, we show that the increased performance of the proposed algorithm uniquely enables it to extract accurate data for the persistence length and end-to-end distance of 107 DNA tethers in a single experiment.

INTRODUCTION

Tracking of individual micron-sized particles by video microscopy has numerous applications in biophysics, particularly in magnetic and optical tweezers (1). One of the main advantages of video microscopy lies in its flexibility, ease of implementation, and ability to track a large number of objects (2). Apart from the camera and image-system hardware, the method is entirely based on software and requires no special hardware like laser-based detection schemes often employed in optical tweezers (3–6). Software can therefore easily be reused and transferred between different applications. Ongoing advances in digital cameras and computing hardware continue to increase the applicability of video microscopy. Megapixel-size cameras now allow the monitoring of thousands of objects, and fast acquisition rates allow cameras to be used for particle tracking in the kHz range (7).

The final resolution of any tracking method depends on the accuracy, which is a measure of the systematic error or bias, and the precision, which is a measure of the statistical error or scatter. With decreasing magnification, the area mapped onto a single pixel increases and the pixel bias, related to mapping of the intensity on the discrete pixel grid, becomes more important than the error due to scatter. High signal/noise ratios are commonly achieved when tracking nondiffraction-limited particles and these often reduce the statistical error well below the error due to bias. There is thus a need for tracking methods that account for this bias such that the bias is reduced to a level below the statistical error or scatter.

The procedure for tracking single fluorophores or other diffraction-limited objects by fitting with the point-spread function of the microscope or an approximation with a two-dimensional Gaussian was recently shown to be capable of achieving the theoretical minimum uncertainty (8,9). However, for objects much larger than the wavelength of light ($d > \lambda$) or for significantly defocused objects, the intensity profile is no longer accurately described by a Gaussian. A different tracking method is therefore required when dealing with such images. A large number of methods have been developed, and they can be roughly divided into two categories: first, methods that perform a direct calculation of the subpixel location (center of mass, Gaussian fit) (10,11); and second, methods that compare the image with another image (be it a predefined kernel, a mirror image, or a previous image) and perform a subsequent fitting step to achieve subpixel resolution. These methods include cross correlation and the sum of absolute differences (12,13). Several of these tracking methods were compared previously (14) and two-dimensional cross correlation proved to be the preferred method for tracking nondiffraction-limited objects. However, a significant contribution of pixel bias to the final resolution remains for the cross-correlation method, which can severely limit the final tracking resolution.

We may understand the pixel-bias error to be due to a loss of information when an image is sampled on a discrete grid (Fig. 1, *A* and *B*) (15). Information on the distribution of intensity within a single pixel is replaced by the mean intensity at the pixel center. If the spatial frequency spectrum of the image exceeds half the sampling frequency, information is lost according to the Nyquist theorem. For example, the centroid of the original image therefore need not be equal to the centroid of the sampled image. This is illustrated in

Submitted August 24, 2011, and accepted for publication March 29, 2012.

*Correspondence: c.dekker@tudelft.nl

Editor: Charles Wolgemuth.

0006-3495/12/05/2362/10 $2.00

doi: 10.1016/j.bpj.2012.03.073

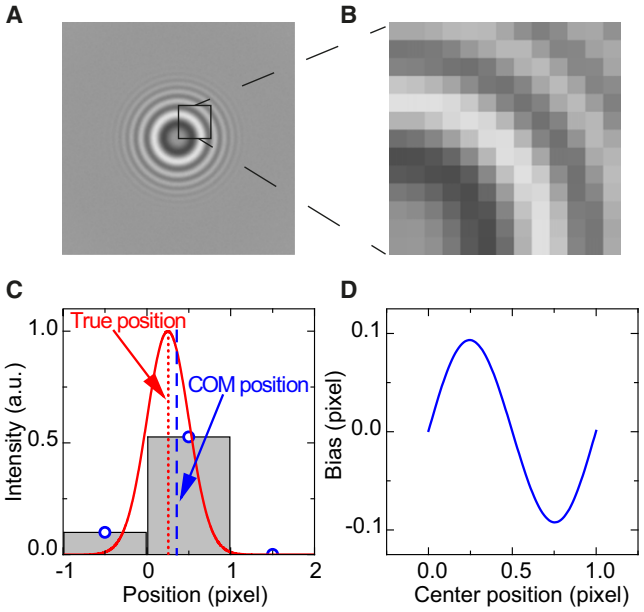

FIGURE 1 Origins of pixel bias. (*A*) Diffraction pattern of a bead. (*B*) Zoom-in on the diffraction pattern showing the artifacts created by the sampling process. (*C*) A Gaussian intensity profile (*solid curve*) is sampled by three pixels. The information of the intensity distribution within a pixel is lost by the sampling process and is replaced by a single intensity at the center of the pixel (*circles*). The centroid of the pixel intensities (*dashed line*) can have an error or pixel bias compared to the true center position of the Gaussian (*dotted line*). (*D*) The pixel bias shows a periodic variation when displacing the Gaussian profile across the pixel grid.

Fig. 1 *C*, where a Gaussian intensity profile is sampled by three pixels. The result of the sampling is an error in the position of the centroid calculated using the sampled data with respect to the true centroid position. This error or pixel bias can be substantial and is periodic in the pixel grid (Fig. 1 *D*). Kernel-based tracking methods may suffer in a similar way from pixel bias. To obtain the final position these methods require a subpixel fitting step, where the exact shape of the peak is partly lost in the sampling process, leading to a possible error in its determination (16).

Pixel bias can be reduced by increasing the magnification and thereby sampling well above the Nyquist frequency. This is however not always possible nor desirable as it reduces the field of view and may also decrease contrast. If the exact intensity profile of the tracked object is known, as is the case for diffraction-limited objects, this information can be used to correct for the information loss due to sampling and thus eliminate bias. If, however, the exact intensity profile is not known, the error due to bias will depend on the specifics of the algorithm.

Here, we describe and evaluate what to our knowledge is a new method for tracking micron-sized beads, using an algorithm specifically aimed at reducing the pixel bias, thereby increasing the final tracking resolution. Our quadrant-interpolation (QI) algorithm makes use of the circular geometry of the diffraction pattern to resample the image on a circular grid. The resampling procedure reduces bias in two ways. First, it allows for a degree of upsampling, which increases the spatial sampling frequency, thereby reducing bias. Second, the resampling on the polar grid effectively removes the integer spacing of the pixel grid and thus averages out the errors due to pixel bias. The performance of the algorithm is evaluated by tracking computer-generated images derived from experimental images and comparing with two commonly used methods: center of mass (COM) (14,17) and cross correlation (XCOR) (12,13,18). We evaluate these different methods for scatter, bias, and resolution at different magnifications, as well as the influence of the signal/noise ratio. We validate the improved performance of the presented algorithm for experimental conditions closely matching the simulations. The ability of the new algorithm to accurately track at low magnification uniquely enables highly parallel single-molecule experiments. We show that we were able to obtain accurate persistence length and end-to-end distance data for 107 DNA molecules in a single multiplexed magnetic-tweezers experiment. The QI algorithm thus enables a vast increase in the throughput of single-molecule experiments and thereby enables the study of rare events and the acquisition of large statistical data sets from individual experimental runs.

MATERIALS AND METHODS

Experimental setup

Images, for the experimental data and the artificial image construction, were acquired with a Falcon 1.4M100XDR (Dalsa) camera in 8 bit mode using a Nikon CFI Plan Apo 50× oil immersion (NA 0.9) objective and a collimated green LED as light source. A 300-mm tube lens was used to obtain an effective magnification of 75×. Images were saved in tif format and processed offline using Labview (National Instruments, Austin, TX). A sample of fixed beads was prepared by immobilizing 2.8 μm magnetic beads (Dynal M270, Invitrogen, Carlsbad, CA) on a glass coverslide by baking at 180°C for 10 min and a flow cell was constructed by sandwiching a second coverslide on top using a parafilm spacer. The z-correction factor was determined experimentally by creating a flow cell with a 50-μm gap, which allowed to focus on the top and bottom surfaces. This flow cell was filled with water and immersion oil separated by a thin parafilm barrier. Subsequently, the required displacement of the objective, δz, to achieve focus at the top and bottom surfaces in both immersion oil and water was measured. The correction factor was then simply given by $\delta z_{oil}/\delta z_{water} = 0.8$ for our setup. We note that this correction factor is significantly different from the small-angle approximation based on the index of refraction of the media: $n_{water}/n_{oil} = 1.33/1.51 = 0.88$, which is not valid for objectives with high numerical aperture.

Evaluation procedure and artificial image construction

Tracking algorithms are often evaluated by tracking a stationary object, where the fluctuations in the tracked position are used to estimate the accuracy of the algorithm. Measurements using immobilized beads or markers, however, provide a too-optimistic value of the resolution, as they do not take the systematic errors or pixel bias into account. To measure the true resolution of a tracking algorithm, one must compare the tracked position

with its actual position, which is experimentally complicated but is easily achieved with computer-generated images. We therefore artificially generated images, simulating a stepwise movement of a particle over the image grid, similar to the methods of Cheezum et al. (14).

We used experimentally acquired images to construct artificial images. The advantage of this a posteriori approach is that a close match to experimental images is guaranteed and no information of the imaging system is required. First, images of a 2.8-μm magnetic bead were recorded at 75× magnification for 200 different focal positions separated by 100 nm, by stepwise moving of the objective in z. Next, these images were used to calculate radial intensity profiles at each z-position, resulting in a z-lookup table (Fig. 2 *E*). Typically, a regularly expanding pattern of fringes is visible, which we approximate by the radial expansion of a single intensity-profile function (Fig. 2 *E*, *red line*). A parabolic fit of the brightest fringe was used to map the monotonous expansion of the fringes as a function of defocus (Fig. 2 *E*, *blue dashed line*). By scaling the radial intensity profiles at each defocus position, an average generic radial profile was constructed, which, together with the parabolic fit of the brightest fringe, now suffices to reconstruct a noise-free pattern at any translational (x,y) and defocus (z) position. We thus have generated a perfect, noise-free image of a bead, henceforth referred to as the reference pattern. To simulate the effect of shot noise, Poissonian distributed noise was finally added to the reference pattern (Fig. 2 *F*).

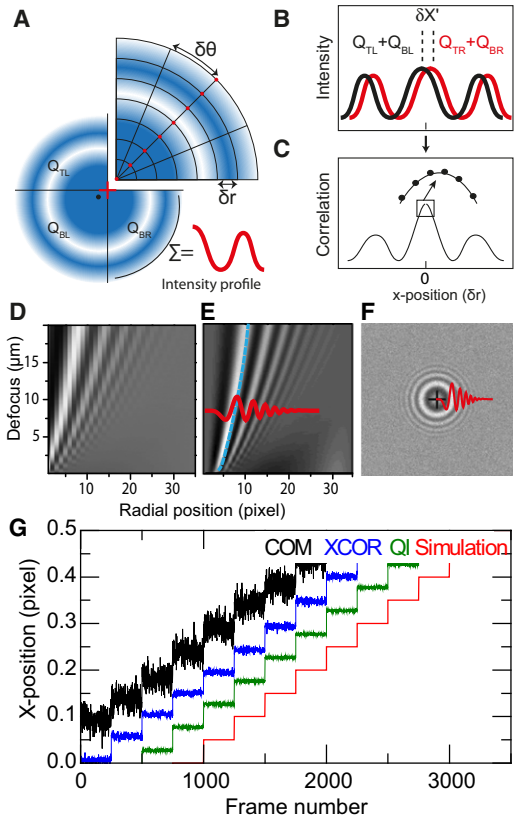

FIGURE 2 Schematic representation of the QI tracking algorithm. (*A*) First, an approximate center position is obtained (*red cross*) by a different tracking method, e.g., COM. Second, radial intensity profiles are constructed by bilinear interpolation on a circular grid with spacing $\delta\theta$, δr. For each quadrant, the intensity profiles are summed to obtain a radial intensity profile for each quadrant (*red curve*). (*B*) Intensity profiles of left/right quadrants are concatenated to represent the pattern in the x-direction (*red curve*), and subsequently, a cross correlation with its mirror image (*black curve*) is performed to obtain the center position of the pattern. (*C*) The peak in the cross correlation is fit to obtain the final x-position. (*D*) z-lookup table of images comparable to Fig. 1 *A* made without interpolation. (*E*) z-lookup table made by summing the radial intensity profiles of four quadrants obtained by interpolation on a circular grid. The brightest fringe was fit by a parabolic function (*blue dashed line*). Using this parabolic fit, all radial intensity profiles were scaled in the radial direction and averaged to create a single generic curve (*red curve*). (*F*) Artificial image generated using the generic curve. Poissonian noise was added to obtain different SNRs. (*G*) Tracking result of simulated images that were regularly displaced by 0.1 pixel in the x-direction at 30× magnification and SNR of 30, offset vertically for clarity: *black*, COM; *blue*, XCOR; *green*, QI; and *red*, actual simulated position.

Next, we generated an image series representing a movement of two pixels across the camera image grid in 40 steps. The z-position of the bead was set at 10 μm above the focal plane, corresponding to the middle of the lookup table. At each step, 250 different images were created by adding shot noise to the initial generated image. The signal/noise ratio (SNR) was subsequently determined from the generated images as

$$SNR = \frac{S}{4\sigma} - 1, \tag{1}$$

where the signal range, S, is defined as the difference between the maximum and minimum intensities of the image, $S = (I_{max} - I_{min})$. The noise is determined from a region of the image containing no signal, where 4σ sets a 95% confidence bound. The factor of 1 is subtracted to account for the apparent increase in the measured signal range due to the addition of noise. Images at different magnifications were obtained by mapping the reference pattern on different pixel grids relative to the 75× magnification of the initial experimental images. Subsequently, these images were tracked with the proposed QI method, as well as with COM and COR algorithms (Fig. 2 *G* (offset for clarity)). The scatter and bias were independently determined. Scatter was calculated as the standard deviation of the tracked position at each step. Bias was calculated as the deviation of the determined mean position from the simulated position minus the overall error in mean position for all steps. Subtracting the overall error in mean position removes any nonposition-dependent difference between the simulated position and tracked position, which is in most practical cases irrelevant, as it will be equal for all tracked objects in a field of view. This approach allows us to determine the bias and scatter separately as a function of the noise, magnification, and z-position of the image.

Tracking software

The QI tracking method was implemented in Labview software. The base tracking algorithm, as well as a standalone program capable of loading and tracking images, is available for download from the author's website: http://ceesdekkerlab.tudelft.nl/download

QUADRANT-INTERPOLATION ALGORITHM

x,y-Tracking

The proposed QI algorithm uses the circular geometry of the diffraction pattern to strongly suppress bias, and it was implemented in Labview software; for details, see Tracking software, above.

The QI algorithm consists of four basic steps to determine the x,y-position:

1. In the first step, the center of the particle is roughly identified by a background-corrected COM (algorithm described in Section S1 in the Supporting Material),

followed by a 1D XCOR (Section S2 in the Supporting Material). The accuracy of this first step is not crucial, and it can be substituted by any method capable of locating the center of the particle to within ~1 pixel (Fig. 2 *A*, *red cross*).

2. The second step uses this first (x_{est}, y_{est})-position to calculate a radial profile of the intensity of the particle for each quadrant on a circular grid, where points are spaced by δr and $\delta\theta$, in radial and angular dimensions, respectively. The values at the circular grid positions are calculated by bilinear interpolation of the four nearest-neighbor pixel values. A single radial-intensity profile is created that represents the quadrant (Fig. 2 *A*). The grid is generally chosen to oversample in the radial direction compared to the pixel size, i.e., $\delta r <$ pixel spacing, and is calculated for each quadrant of the image (i.e., top left, top right, bottom right, bottom left), yielding four intensity profiles $q_{\mathrm{TL}}(r)\ldots q_{\mathrm{BL}}(r)$. These four radial profiles will be used to determine both the *x*,*y*- and the *z*-position.

3. In the third step, relative shifts in the radial profiles are used to extract a correction to the initial (x_{est}, y_{est})-position. The sum of the right profiles, $q_{\mathrm{R}} = q_{\mathrm{TR+BR}}$, is concatenated with the left equivalent $q_{\mathrm{L}} = q_{\mathrm{TL+BL}}$, thus creating an intensity profile, I_x, that represents the horizontal shift,

$$I_x(r) = q_L(-r) \parallel q_R(r), \tag{2}$$

where $\parallel$ denotes the concatenation (Fig. 2 *B*). The resulting intensity profile, $I_x(r)$, is now cross correlated by Fourier transform with its mirror profile, $I_x(-r)$,

$$X_{xx'}(r) = \mathrm{IFFT}(\mathrm{FFT}(I_x(r)) \times \overline{\mathrm{FFT}(I_{x'}(-r))}), \tag{3}$$

where IFFT and FFT are the inverse and regular fast Fourier transforms, respectively, and $\overline{\mathrm{FFT}(I_{x'}(-r))}$ denotes the complex conjugate. The resulting cross-correlation function $X_{xx'}(r)$ is a curve with spacing δr and a peak at the position corresponding to twice the displacement δ_r of the particle from the center of the circular grid. A similar routine is followed in the *y*-direction by processing $q_{\mathrm{T}} = q_{\mathrm{TL+TR}}$ and $q_{\mathrm{B}} = q_{\mathrm{BL+BR}}$.

4. The final step in the algorithm determines the sub-bin peak position with a five-point parabolic fit to the correlation function, yielding a shift of δ_r (Fig. 2 *C*). For corrections smaller than one pixel unit, i.e., small compared to the radial pattern fringe spacing, δ_r relates to a truly *x*-directed pattern shift, δ_x, via a simple geometrical correction, $\delta_x = \delta_r/(\pi/2)$, which accounts for the summation of the profiles, and their cosine-projected displacements, over a hemisphere. The tracked position thus finally is $x = x_{est} - \delta_x$. The *y*-position is calculated analogously.

The second step of the algorithm, where radial intensity profiles are calculated, allows a choice of the parameters of the polar grid, $\delta\theta$ and δr. In general, the final resolution increases with a higher sampling density in the radial direction (i.e., smaller δr). However, empirically we have found that the final resolution does not increase further when δr is reduced below $\approx 1/3$ of a pixel unit. The angular spacing, $\delta\theta$, is chosen to sample all pixels, i.e., $\delta\theta \times r_{max} =$ pixel size, where r_{max} is the maximum radius used to construct the radial intensity profile. The final resolution does not improve if $\delta\theta$ is decreased further. However, $\delta\theta$ may be increased considerably without severe loss in tracking resolution. This enables one to trade off accuracy for speed by sampling on a more widely spaced grid. The execution speed of the algorithm, when sampling all pixels, is sufficient for most applications and in its current implementation is ~0.01 s for a 128 × 128-pixel image on a 2-GHz Intel core2 CPU.

z-Tracking algorithms

Methods for tracking the axial or *z*-position of a particle generally rely on first creating a lookup table of radial profiles by shifting the objective in known steps (13,19). Here, we employ the following method: an image stack is acquired by changing the focus of the objective, typically in 200 steps of 100 nm. Subsequently, a *z*-lookup table is constructed by calculating the radial profile at each focus position. For the COM method, the pixel intensities were directly mapped into radial bins with 1-pixel spacing (Fig. 2 *D*). For the XCOR method, the pixel intensities were distributed by linear interpolation into radial bins with 1-pixel spacing. For the QI tracker, the radial profiles, calculated using bilinear interpolation over four quadrants with a δr of 1/3 pixel, were averaged, resulting in a much smoother lookup table (Fig. 2 *E*).

To determine the *z*-position for a given image, the χ^2-difference of the radial profile with the planes of the *z*-lookup table was calculated. The minimum of the χ^2-difference corresponds to the best matching radial profile and therefore to the *z*-position of the object. To achieve a resolution smaller than the step size of the lookup table, the final *z*-position was obtained by a parabolic fit of this minimum. When using an oil-immersion objective, the refractive index of the immersion medium is normally not equal to the refractive index of the medium containing the tracked object. Therefore, a displacement of the objective, used to make the *z*-lookup table, is not equivalent to a displacement of the object during a measurement (20). We use an experimentally determined linear correction factor (0.80 for our system, see Materials and Methods), to correct for this scaling of the *z*-position.

RESULTS

Using the procedure outlined above, we evaluated the influence of magnification, SNR, and cross talk on tracking of nondiffraction-limited particles. We compare the newly developed QI algorithm to the well-established COM and XCOR methods. In the results below, the standard deviation, σ, is shown in units of pixels at different magnifications for scatter and bias. An example of the scatter and bias at 75× magnification is shown in Fig. 3 *B*. The total resolution was subsequently calculated from the bias, σ_{bias}, and scatter, $\sigma_{scatter}$, at each magnification as

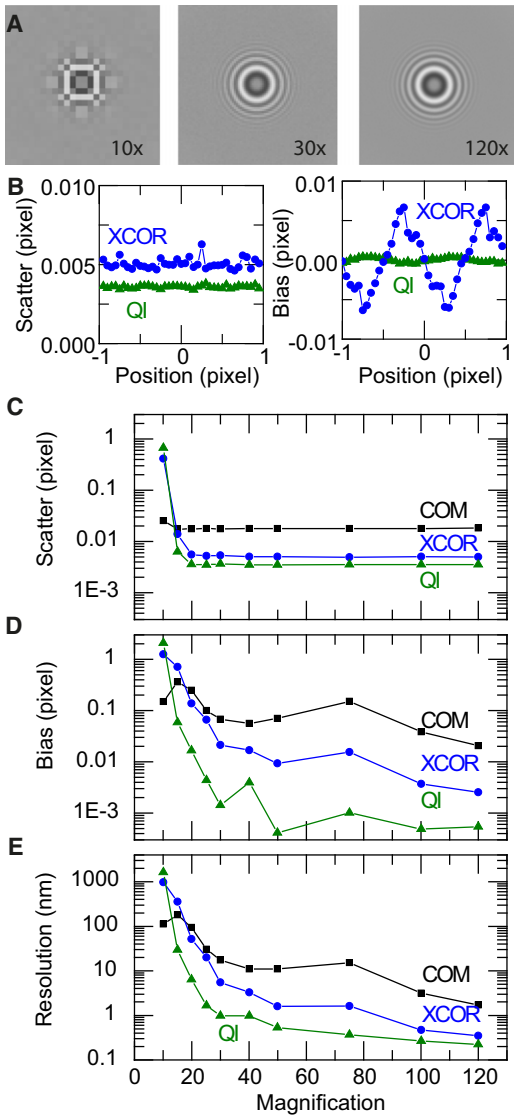

FIGURE 3 Scatter, bias, and resolution in the *x*-direction for simulated data as a function of magnification at an SNR of 30. (*A*) Simulated images at different magnifications. (*B*) Examples of scatter and bias at 75× magnification for a displacement across two pixels. (*C*) Scatter as a function of magnification. (*D*) Bias as a function of magnification. The error due to pixel bias was comparable to scatter for COM and XCOR, but significantly reduced for the QI tracker. (*E*) Resolution in nanometers for a 7.5-μm pixel size as a function of magnification.

$$\sigma_{total} = \sqrt{\sigma_{bias}^2 + \sigma_{scatter}^2} \tag{4}$$

and is shown in nanometers for the given magnification based on a 7.4-μm pixel size, matching the pixel size of the camera used to obtain the experimental images. Unless stated otherwise, all results were evaluated at an SNR of 30.

The experimentally obtainable maximum signal/noise level for an 8-bit camera can be estimated to be a~30, based on the signal range and expected shot noise. The maximum peak-to-peak signal range, S, without clipping, will be approximately half the bit depth i.e., $S = 128$ for the 8-bit camera. Assuming a pixel-well depth of 100,000e for a typical camera, the shot noise calculated for the median intensity of 50,000e will be $\sigma = 256/\sqrt{50000} \approx 1.1$ bit, which results in a signal/noise ratio of $SNR = S/(4\sigma) \approx 28$. Higher SNRs can be obtained by using cameras with a larger pixel-well depth and using cameras capable of working at more than 8-bit. However, in most cases, shot noise will be limiting, as it is generally larger than 0.5 bit.

x,*y*-Tracking

The results for in-plane tracking show that the stochastic error or scatter remains nearly constant for all three algorithms (Fig. 3 *C*). Only at magnifications below 20× does the scatter increase markedly for both the XCOR and QI tracker, which likely results from undersampling of the spatial pattern. Above 15× magnification, the QI tracker has improved performance compared to both COM and XCOR algorithms.

Bias performance is more sensitive than scatter performance to magnification for all algorithms, and there are larger differences in tracking error between the tracking algorithms (Fig. 3 *D*). As expected, bias decreases with magnification, as the image is spread out over more pixels, reducing the effect of pixel borders. The QI algorithm shows a fast decrease in bias, reaching a low-bias region above 50× magnification. Bias for the COM and XCOR methods reduces more slowly with magnification and never reaches the performance of the QI method. It is important to note that the bias for the COM and XCOR algorithms is larger than the scatter for most magnifications, thereby limiting the total resolution (Fig. 3 *E*). In the absence of bias, the resolution of all tracking algorithms would improve linearly with magnification, as scatter measured in pixels stays constant. However, the bias significantly affects performance, especially for the COM and XCOR tracking routines. The QI algorithm shows superior performance, because it is not bias-limited and resolution indeed scales with magnification from 30× upwards, where scatter is the main source of error.

z-Tracking

Tracking resolution in the *z*-direction is generally less than the *x*,*y*-resolution, as the expansion of the diffraction pattern

changes only slowly with z-position (Fig. 2, *D* and *E*). Our system has ~1 nm radial expansion for a 7-nm z-displacement, as calculated from the local slope of the fringe pattern in the z-lookup table. The resolution in z was evaluated by a simulated displacement over 2 μm in 100 steps at constant x,y-position. The result is shown in Fig. 4 *A*: the QI algorithm achieves a resolution below 10 nm for magnifications >25×. The COM and XCOR algorithms perform less well, which is due to propagation of x,y-tracking errors. Using the more accurate x,y-positions obtained from the QI tracker as input for the COM- and XCOR-based z-tracking algorithms showed improved performance, comparable to that of the QI z-tracking methods (data not shown), which underlines the importance of accurate x,y-tracking for accurate z-tracking.

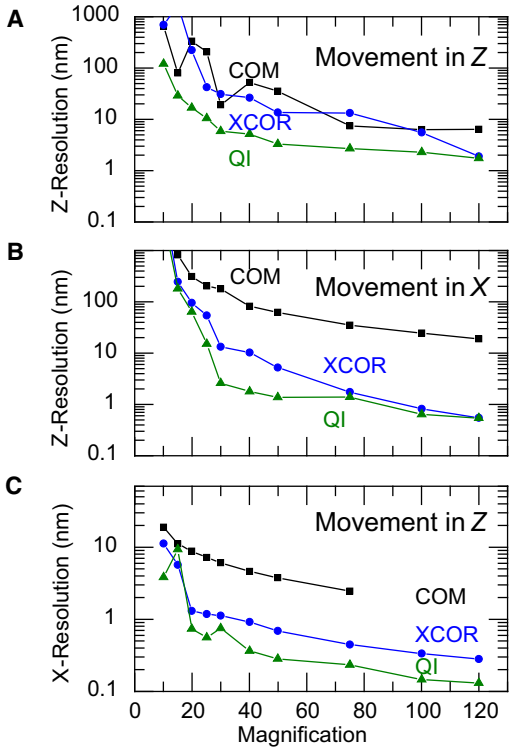

D

		Move X	Move Y	Move Z	Total
X-Resolution (nm)	**QI**	**0.4**	**0.2**	**0.2**	**0.5**
	XCOR	1.6	0.4	0.4	1.7
	COM	15.2	1.8	2.4	15.5
Z-Resolution (nm)	**QI**	**1.4**	**1.4**	**2.7**	**3.3**
	XCOR	1.6	1.6	6.7	7.8
	COM	35.1	35.1	7.5	50.2

FIGURE 4 (*A–C*) Axial resolution and cross talk between x- and z-positions as a function of magnification for simulated data at an SNR of 30, showing z-resolution determined for a 2-μm z-movement of the bead (*A*); cross talk in z-tracking for a stepwise displacement over 2 pixels in the x-direction for the tracked bead, where displacements in x result in significant performance loss for the noninterpolating COM tracking method (*B*); and cross talk in the x-direction for a simulated bead movement of 2 μm in z (*C*). *Squares*, COM; *circles*, XCOR; *triangles*, QI. (*D*) Cross talk in tracking resolution in nanometers at 75× magnification and an SNR of 30. Columns show the direction of movement for the tracked bead. The last column shows the total resolution calculated as $\delta x_{total} = \sqrt{\delta x^2_{moveX} + \delta x^2_{moveY} + \delta x^2_{moveZ}}$, or $\delta z_{total} = \sqrt{\delta z^2_{moveX} + \delta z^2_{moveY} + \delta z^2_{moveZ}}$.

To evaluate the cross talk between in-plane tracking and z-tracking, we evaluated the z-resolution while displacing the bead image in the x-direction at constant z-position (Fig. 4 *B*). The QI algorithm again shows the best performance at all magnifications. The COM noninterpolating z-tracking algorithm performs more than an order of magnitude worse than the interpolating QI and XCOR methods. This very large error is due to the noninterpolating z-tracking algorithm used for the COM tracker, which simply maps the intensity of a pixel to 1-pixel-wide bins in the radial intensity profile. The XCOR z-tracker, on the other hand, uses linear interpolation to distribute the intensity between two radial bins and performs significantly better. If the noninterpolating COM z-tracking method was used in the XCOR algorithm, performance decreased notably, becoming comparable to that of the COM (data not shown). Interpolation of the radial profile thus enables much better suppression of in-plane movements, irrespective of the tracking algorithm used.

Finally, we also evaluated the sensitivity of the x-resolution with respect to movements in z (Fig. 4 *C*). The cross talk in this case is small compared to the error for in-plane movements. Therefore, the x,y-resolution will generally only have a minor contribution from cross talk due to z-movements. At very low magnifications, both the QI and XCOR methods show a strong degradation of resolution, as the diffraction pattern is not correctly sampled anymore.

The above results demonstrate that the resolution in tracking of an object moving in three dimensions can be dramatically worsened by cross talk present between movements in the x,y- or the z-direction. To gain further insight into the effects of cross talk, we calculated the resolution in individual x,y- and z-directions, as well as the total resolution at 75× magnification with an SNR of 30 (Fig. 4 *D*). This shows that the QI tracker has the lowest level of absolute cross talk, and that XCOR and COM have higher levels of absolute cross talk in the x,y-direction. Most notable is the very severe cross talk between x,y-movements and z-tracking, resulting in a significantly reduced performance for the noninterpolating COM z-algorithm.

Signal/noise ratio

To determine the performance of the tracking methods as a function of SNR, we evaluated the resolution at SNRs between 2 and 100, as defined in Eq. 1 at a constant magnification of 75×. As expected, the scatter decreases monotonically with increasing SNR (Fig. 5 *A*, *solid symbols*). At low SNR, the QI method performs better compared to XCOR, which is explained by the fact that it samples all pixels, whereas XCOR only samples a subset, resulting

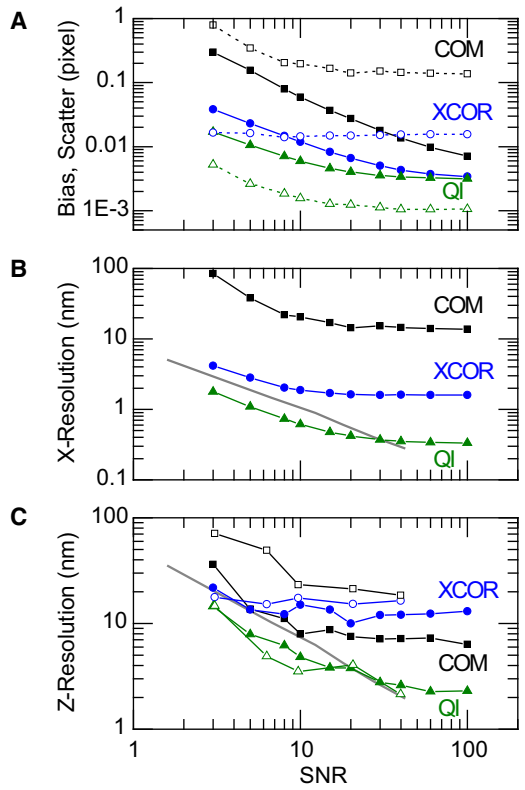

FIGURE 5 Influence of the SNR at 75× magnification. (*A*) Scatter (*solid lines and symbols*) and bias (*dashed lines and open symbols*) for simulated data in the *x*-direction as a function of SNR, for the COM (*squares*), XCOR (*circles*), and QI (*triangles*) algorithms. Scatter decreased monotonically with increasing SNR for all algorithms. The bias for both the COM and XCOR methods was larger than their scatter for most SNRs, thus negatively dominating the final resolution. The bias of the QI algorithm was well below scatter for all SNRs, resulting in a superior total resolution. (*B*) *x*-resolution as a function of SNR for the simulated data. Bias heavily affects performance of the COM and XCOR algorithms. The resolution prediction calculated for the experimental images (*gray line*; see Section S3 in the Supporting Material) agrees with the simulation results within a factor of 2 over the whole range of SNRs. (*C*) *z*-resolution as a function of SNR for simulated (*solid symbols*) and experimental data (*open symbols*). Experimental results for both QI and XCOR algorithm agree well with the simulation results. The resolution prediction calculated for the experimental images (*gray line*; Section S3 in the Supporting Material) matches well with the experimental data.

in higher effective noise. The bias (Fig. 5 *A*, *open symbols*) is influenced in a more complex way by the SNR: COM and QI show a decrease in bias with increasing SNR. The bias for the XCOR is, however, independent of the SNR. It is important to note that the bias for the COM and XCOR methods is larger than the scatter for most SNR, and bias thus dominates the total resolution (Fig. 5 *B*).

To gain insight into the general effects of magnification and SNR on tracking resolution, we developed a simple analytical expression of the achievable resolution that is based on the signal amplitude and SNR of an image (method outlined in Section S3 in the Supporting Material). This prediction (Fig. 5 *B*, *gray line*) reproduces the SNR behavior of the QI tracker within a factor of 2 for SNR < 40. For higher SNRs, the resolution of the QI levels off and does not match the prediction anymore. Next, we evaluated the SNR response for *z*-tracking (Fig. 5 *C*). *z*-resolution again improves with the SNR for all methods. The QI algorithm performs best for all SNRs, whereas the noninterpolating *z*-algorithm of the COM tracker has a severely reduced resolution. We extended the resolution prediction to the *z*-direction by scaling the predicted *x*-resolution with a factor of 7, equal to the relative expansion of the diffraction pattern in the radial direction for a given focus displacement. This simple scaling indeed approximates the behavior of the *z*-resolution of the QI tracker (Fig. 5 *C*, *gray line*).

Experimental validation

To validate the simulation approach and the performance of the QI tracker, we performed an experiment that closely matched the simulations. The *z*-resolution was measured for a *z*-displacement at different SNRs. To create a *z*-displacement, the objective was moved in 20 steps of 100 nm, matching the 2 μm total displacement used in the simulations. Magnetic beads identical to those used to generate the reference image for the simulations (2.8 μm) were immobilized on a glass coverslide, and tracking resolution of the different algorithms was evaluated at 75× magnification as a function of SNR (Fig. S4). The SNR was set in the range between 3 and 40 by changing the illumination intensity. To remove experimental drift, a single bead was used as a reference. The tracked position of this reference bead was subsequently subtracted for each time point from the positions of the other beads ($n = 4$). The resolution was calculated as the standard deviation of the reference-subtracted bead positions divided by $\sqrt{2}$, to account for the noise added by subtracting the reference bead (21). These experimental results provide a lower limit for the resolution and closely match the simulation results for the QI and XCOR algorithms (Fig. 5 *C*, *open symbols*). The experimental resolution of the COM algorithm (Fig. 5 *C*, *black open symbols*) shows markedly worse performance than the results from the simulations. This can be explained by the fact that the COM algorithm is very sensitive to disturbances such as uneven background illumination or asymmetries in the tracked beads. Both of these effects are present in the experimental data but not in the simulated, thereby decreasing the observed experimental tracking resolution. The simple resolution estimate outlined in Section S3 in the Supporting Material (Fig. 5 *C*, *gray line*) matches both the experimental and simulated data within a factor of 2. The above results show that under near identical conditions, the *z*-resolution of the experimental data match closely the simulation results, validating the evaluation approach based on simulations.

The QI algorithm enables highly parallel magnetic tweezers

To demonstrate the experimental relevance of the proposed QI algorithm, we performed measurements at 25× magnification in multiplexed magnetic tweezers. Targeted DNA tethering was used to tether a large number of 1-μm paramagnetic beads to 7.3-kb DNA molecules in a 10 mM Tris buffer (pH 7.5) (Fig. 6 *A*) (22). Using this technique we were able to identify 245 individual beads in the 300 × 400-μm field of view. A measurement procedure optimized to efficiently handle a large number of the DNA tethers in a single experimental run was used to obtain force extension characteristics ((22,23) and I. De Vlaminck, T. Henighan, M. T. J. van Loenhout, D. R. Burnham, and C. Dekker, unpublished). The COM, XCOR, and QI algorithms were used in parallel to obtain tracking data during these measurements and evaluate the performance of each algorithm. The tracking results for a force-extension measurement of a single DNA tether reveal that only the QI algorithm is able to accurately track the bead position throughout this force-extension measurement (Fig. 6 *B*). The COM algorithm loses tracking completely for most data points; whereas the XCOR algorithm manages to track the bead for most positions but suffers from large discrete steps in the tracked position, resulting in large errors and an overestimation of the DNA length.

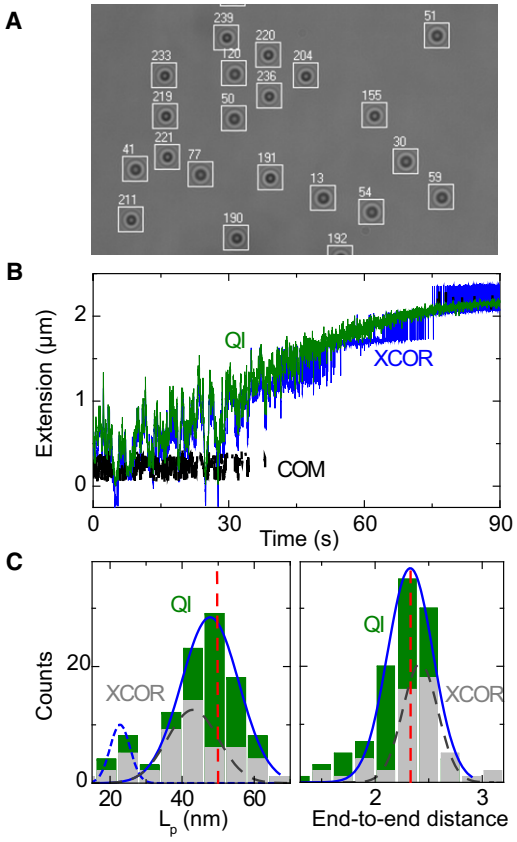

FIGURE 6 Tracking in highly parallel multiplexed magnetic tweezers at 25× magnification. (*A*) Part of a field of view in a multiplexed magnetic tweezers setup showing multiple beads at low resolution; in the total field of view, 245 beads were identified. (*B*) Tracking results for the three different trackers of an experimental DNA force-extension curve. The force applied on the bead was changed from ~20 fN at $t = 0$ s, to 3 pN at $t = 90$ s. The large errors of the COM and XCOR algorithms show their failure at low magnification. (*C*) Persistence lengths and end-to-end distances extracted from analysis of beads tracked with the QI (*green bars*) and XCOR algorithms (*gray bars*). Two peaks are found for the persistence length, corresponding to single and double tethered DNA molecules (*blue solid and dashed lines*, QI; *black dashed line*, XCOR). The persistence lengths and end-to-end distances determined by the QI algorithm are close to the expected values (*red dotted lines*).

To evaluate the quality of the data obtained by the different tracking algorithms, we performed an analysis of the end-to-end length of 7.3-kb DNA molecules and their persistence length (L_p), a measure for the length scale over which orientational fluctuations decay. Out of all the beads tracked, the QI algorithm yielded 107 DNA tethers that could be fit by the wormlike chain model (25,26). Only 51 tethers tracked by XCOR algorithm could be fit and none of the tethers tracked by the COM algorithm provided useful data. The results for the obtained L_p and end-to-end distance of the DNA molecules are shown in Fig. 6 *C*. The histogram of L_p for the QI tracker shows two peaks, one at 48 nm and one at 23 nm, corresponding to beads tethered by a single DNA molecule and beads tethered by two molecules (27). The measured L_p obtained by the QI algorithm is in good agreement with previous measurements by which it was determined that $L_p \approx 50$ nm and is modestly dependent on salt in the range of 30 mM to 150 mM Na^+ (25). The histogram for the persistence length, determined from the data of the XCOR algorithm, showed a peak at 43 nm, considerably lower than the expected value of 50 nm.

A histogram of the measured end-to-end distance of the DNA molecules is shown in Fig. 6 *C*. The end-to-end distance at a nominal force of 1.8 pN was obtained by measuring the bead height for 25 s at a nominal force of 1.8 pN. The peak found for the QI algorithm at 2.33 ± 0.18 μm is close to the expected length of 2.26 ± 0.005 μm (at 1.8 pN, 25-s measurement time). The peak for the XCOR algorithm was located at a distance of 2.42 ± 0.14 μm, longer than the expected end-to-end distance. The increase in end-to-end distance determined by the XCOR algorithm can be understood by looking at the tracked bead positions in Fig. 6 *B*. The tracking errors made by the XCOR algorithm lead to an underestimation of the lowest positions and an overestimation of the largest extensions, resulting in a longer measured end-to-end distance.

DISCUSSION

In this work, we have developed to our knowledge a novel algorithm for tracking of nondiffraction-limited objects in 3D. We have demonstrated superior performance of this

newly developed QI algorithm compared to the COM and XCOR algorithms. In particular, the QI algorithm leads to a reduction of bias and reduced cross talk between x,y- and z-motions. The properties of the QI algorithm allow it to function at high precision and at low magnification. The QI algorithm enables large-scale multiplexed single-molecule measurements on DNA tethers where other algorithms fail.

The difference in bias performance between the algorithms depends on how they deal with the information loss due to sampling. The point-spread function of the microscope sets an upper limit for the spatial frequency components of the image. For a perfect aberration-free objective lens, the point-spread function in the focal plane takes the form of an Airy disk. The Airy disk has a diameter of $d_a = 1.22\ \lambda/NA = 705$ nm, where $\lambda = 520$ nm and NA $=$ 0.9 in our setup. Fourier analysis of the Airy pattern shows that 99% of the information is contained in spatial frequencies >350 nm. Applying the Nyquist criterion to the Airy pattern gives a minimum required sampling resolution of 350 nm/2 = 175 nm, which corresponds to 42× magnification in our setup. This shows that the QI tracking method makes effective use of all the information in the sampled image, as bias does not improve for magnifications >50×. The COM and XCOR algorithms, on the other hand, do not suppress bias well and require magnifications well above the Nyquist criterion to reduce bias.

A notable feature for all trackers was the sharp decrease in resolution at magnifications <20×. This loss of tracking is also related to the spatial information content of the image. In this case, however, it is linked to the fringes in the diffraction pattern, which account for the main information component in the image. As the fringe spacing approaches the pixel size, a severe loss of information occurs, resulting in major tracking errors. The fringe spacing between the main and second fringes in the generated images was ~1.3 μm, which corresponds to a sampling limit at a magnification of 12×, matching well with the observed loss in resolution for magnifications <20× (Fig. 3 *E*).

The resolution in z is considerably lower than the x-resolution, due to the fact that the diffraction pattern only expands slowly with movements in z. Indeed, the analytical expression for the achievable resolution (see Section S3 in the Supporting Material) correctly captures the z-resolution by simply scaling the predicted x-resolution by a factor equal to the relative radial expansion of the diffraction pattern for a given axial displacement of the particle (Fig. 4 *C*). To increase z-resolution, it would thus be necessary to make the diffraction pattern more sensitive to changes in z. This can be achieved by simply increasing magnification or the numerical aperture of the objective; moreover, interference-based measurements are able to greatly increase the sensitivity to z-displacements and have indeed successfully been applied to increase z-resolution (18,28).

The tracking resolution for particles moving in multiple dimensions can suffer from cross talk. We showed that z-tracking especially can be significantly affected by cross talk of in-plane movements (Fig. 4 *B*), as in-plane tracking errors will broaden and deform the radial profile. By using interpolation to create the radial intensity profile, the QI and XCOR methods suppress pixelation deformations, resulting in a much improved z-resolution. In experimental conditions, the effects of cross talk may easily go unnoticed; tracking fixed beads will not reveal the errors due to cross talk, but particles undergoing Brownian fluctuations will exhibit strong cross talk. Simulations are thus essential to verify the performance of algorithms.

Single-molecule measurements are often not limited by resolution but are constrained by the number of events that can be recorded in a single run. Multiplexing of the measurements is therefore highly desirable, and several approaches for doing so have been published (21,29). Reducing magnification allows more beads to be imaged and tracked. It is therefore interesting to compare the tradeoff between tracking resolution and magnification. The tracking resolution scales approximately linearly with magnification, but the number of beads scales as the square of the inverse resolution. Decreasing the magnification thus provides a means to track many more beads at a limited loss of resolution. The Nyquist frequency, however, sets a limit to the minimal magnification that is allowed before a major loss in resolution occurs. Our results show that at 30× magnification, a sub-1-nm resolution for x,y-direction and a sub-10-nm resolution for the z-direction are possible. These resolutions, only achieved with the QI tracker, are more than sufficient for many single-molecule experiments. Decreasing the magnification to 30× allows 11 times more beads/area to be tracked compared to a 100× magnification.

Several additional sources of error exist that were not considered in this work. These include camera errors and pixel nonlinearity, which have been shown to influence tracking of single fluorophores (30), as well as mechanical and acoustical vibrations, or an uneven illumination and background. Particles may also be nonspherical. The QI tracking algorithm is, however, robust to such deformations of the circular geometry if these remain well below the fringe spacing in the diffraction pattern. With proper care, it should be possible to reduce these sources of error and obtain results similar to those of the simulations, as indeed is shown in our experimental validation.

We have optimized the settings for each algorithm and believe that the results are representative for the general performance of each method. The clear performance trends increase our understanding of the underlying mechanisms. Many different algorithms and variations are used in the literature, and results may differ depending on specific parameters. Claims in literature about the obtained resolution should therefore always be treated carefully, as they often provide an indication of performance only under specific

conditions, e.g., for static objects, where bias or cross talk may go unnoticed.

We showed that under many circumstances, the tracking resolution of nondiffraction-limited particles is limited by bias and cross talk. Simulations are essential to understand these effects and provide a means to evaluate and select a tracking algorithm with superior performance. We have shown that multiplexed magnetic tweezers using the QI algorithm were able to provide vastly more data, obtaining a full histogram of L_p and end-to-end distances in a single experimental run. Not only did the QI tracker allow us to obtain data for more than twice the number of DNA tethers compared to the XCOR algorithm, but, of greater importance, its superior tracking resolution proved essential for obtaining correct physical properties for the measured DNA molecules. We highly recommend the use of the QI algorithm for tracking nondiffraction-limited spherical particles, as it operates with very low bias and cross talk and thereby achieves a higher final resolution in three dimensions. It is especially useful in conditions that are normally affected by bias, i.e., when tracking multiple beads at low magnification or when working at high SNRs.

SUPPORTING MATERIAL

Four sections, including a figure, and references are available at http://www.biophysj.org/biophysj/supplemental/S0006-3495(12)00453-5.

REFERENCES

1. Neuman, K. C., and A. Nagy. 2008. Single-molecule force spectroscopy: optical tweezers, magnetic tweezers and atomic force microscopy. *Nat. Methods.* 5:491–505.
2. Crocker, J. C., and B. D. Hoffman. 2007. Multiple-particle tracking and two-point microrheology in cells. *In* Cell Mechanics. Y. Wang and D. Discher, editors. Elsevier Academic, San Diego. 141–178.
3. Ghislain, L. P., N. A. Switz, and W. W. Webb. 1994. Measurement of small forces using and optical trap. *Rev. Sci. Instrum.* 65:2762–2768.
4. Simmons, R. M., J. T. Finer, …, J. A. Spudich. 1996. Quantitative measurements of force and displacement using an optical trap. *Biophys. J.* 70:1813–1822.
5. Rohrbach, A., and E. H. K. Stelzer. 2002. Three-dimensional position detection of optically trapped dielectric particles. *J. Appl. Phys.* 91:5474–5488.
6. Huisstede, J. H. G., K. O. van der Werf, …, V. Subramaniam. 2005. Force detection in optical tweezers using backscattered light. *Opt. Express.* 13:1113–1123.
7. Otto, O., F. Czerwinski, …, U. F. Keyser. 2010. Real-time particle tracking at 10,000 fps using optical fiber illumination. *Opt. Express.* 18:22722–22733.
8. Smith, C. S., N. Joseph, …, K. A. Lidke. 2010. Fast, single-molecule localization that achieves theoretically minimum uncertainty. *Nat. Methods.* 7:373–375.
9. Mortensen, K. I., L. S. Churchman, …, H. Flyvbjerg. 2010. Optimized localization analysis for single-molecule tracking and super-resolution microscopy. *Nat. Methods.* 7:377–381.
10. Brown, L. G. 1992. A survey of image registration techniques. *ACM Comput. Surv.* 24:325–376.
11. Berglund, A. J., M. D. McMahon, …, J. A. Liddle. 2008. Fast, bias-free algorithm for tracking single particles with variable size and shape. *Opt. Express.* 16:14064–14075.
12. Gelles, J., B. J. Schnapp, and M. P. Sheetz. 1988. Tracking kinesin-driven movements with nanometre-scale precision. *Nature.* 331: 450–453.
13. Gosse, C., and V. Croquette. 2002. Magnetic tweezers: micromanipulation and force measurement at the molecular level. *Biophys. J.* 82:3314–3329.
14. Cheezum, M. K., W. F. Walker, and W. H. Guilford. 2001. Quantitative comparison of algorithms for tracking single fluorescent particles. *Biophys. J.* 81:2378–2388.
15. Alexander, B. F., and K. C. Ng. 1991. Elimination of systematic-error in subpixel accuracy centroid estimation. *Opt. Eng.* 30:1320–1331.
16. de Jong, P. G. M., T. Arts, …, R. S. Reneman. 1990. Determination of tissue motion velocity by correlation interpolation of pulsed ultrasonic echo signals. *Ultrason. Imaging.* 12:84–98.
17. Carter, B. C., G. T. Shubeita, and S. P. Gross. 2005. Tracking single particles: a user-friendly quantitative evaluation. *Phys. Biol.* 2:60–72.
18. Kim, K., and O. A. Saleh. 2009. A high-resolution magnetic tweezer for single-molecule measurements. *Nucleic Acids Res.* 37:e136.
19. Zhang, Z. P., and C. H. Menq. 2008. Three-dimensional particle tracking with subnanometer resolution using off-focus images. *Appl. Opt.* 47:2361–2370.
20. Hell, S., G. Reiner, …, E. H. K. Stelzer. 1993. Aberrations in confocal fluorescence microscopy induced by mismatches in refractive-index. *J. Microsc.* 169:391–405.
21. Ribeck, N., and O. A. Saleh. 2008. Multiplexed single-molecule measurements with magnetic tweezers. *Rev. Sci. Instrum.* 79:094301.
22. De Vlaminck, I., T. Henighan, …, C. Dekker. 2011. Highly parallel magnetic tweezers by targeted DNA tethering. *Nano Lett.* 11:5489–5493.
23. Kruithof, M., F. Chien, …, J. van Noort. 2008. Subpiconewton dynamic force spectroscopy using magnetic tweezers. *Biophys. J.* 94:2343–2348.
24. Reference deleted in proof.
25. Marko, J. F., and E. D. Siggia. 1995. Stretching DNA. *Macromolecules.* 28:8759–8770.
26. Bustamante, C., J. F. Marko, …, S. Smith. 1994. Entropic elasticity of lambda-phage DNA. *Science.* 265:1599–1600.
27. Charvin, G., A. Vologodskii, …, V. Croquette. 2005. Braiding DNA: experiments, simulations, and models. *Biophys. J.* 88:4124–4136.
28. Shtengel, G., J. A. Galbraith, …, H. F. Hess. 2009. Interferometric fluorescent super-resolution microscopy resolves 3D cellular ultrastructure. *Proc. Natl. Acad. Sci. USA.* 106:3125–3130.
29. Ramanathan, S. P., K. van Aelst, …, R. Seidel. 2009. Type III restriction enzymes communicate in 1D without looping between their target sites. *Proc. Natl. Acad. Sci. USA.* 106:1748–1753.
30. Pertsinidis, A., Y. X. Zhang, and S. Chu. 2010. Subnanometre single-molecule localization, registration and distance measurements. *Nature.* 466:647–651.